

Network Modeling as a Tool for Petrophysical Measurements in Chalk

M.S. Talukdar^{1,2}, M. Ioannidis³, J. Howard⁴, O. Torsaeter¹

¹Norwegian University of Science and Technology, Norway; ²Norsk Hydro ASA, Norway; ³University of Waterloo, Canada; ⁴Phillips Petroleum Company, USA

Abstract

We report on a study aimed at generating and characterizing stochastic models of the porous microstructure of chalk. Such models are constructed exclusively from limited morphological information obtained from 2D backscatter SEM images of the microstructure. Two different stochastic reconstruction methods are considered: conditioning and truncation of Gaussian random fields (GRF) and simulated annealing (SA). The potential of initializing the SA reconstruction with input generated using the GRF method is evaluated. It is found that this practice accelerates significantly the rate of convergence of SA reconstruction. This finding is important because the main advantage of SA method, namely its ability to impose a variety of reconstruction constraints, is usually compromised by its very slow rate of convergence.

A detailed description of the chalk microstructure in the form of 3D volume data is essential for the prediction of petrophysical properties from first principles. Here we first consider the prediction of absolute permeability and formation factor directly from such information. We then consider the prediction of absolute permeability, formation factor, mercury-air drainage capillary pressure curve and resistivity index vs. water saturation relationship using approximate network models constrained by information (pore and throat size distributions, coordination number) obtained from geometric and topological analysis of the reconstructed pore networks. Such information is extracted from the 3D volume data using morphological skeletonization and pore space partitioning methods. Very good agreement between the predicted and measured data is found for a sample of North Sea chalk. On the basis of these findings, it is concluded that (a) stochastic reconstruction reproduces the essential features of pore geometry and connectivity of the sample under study, and (b) the network modeling approach used preserves the essential features of pore geometry and connectivity of the reconstructed pore space.

1. Introduction

By comparison to methods based on direct solution of the relevant transport equations in complex 3D pore geometries (e.g., Stokes' equation for single phase flow), network models provide a computationally efficient way to predict a variety of petrophysical properties from pore structure information. The requisite information (pore and throat shape and size distributions, pore-to-pore connectivity and spatial correlation) is, however, quite difficult to determine. A description of the pore space of the medium under consideration in the form of 3D volume data is required for both direct computation of transport properties and for extracting key geometric and topological parameters needed by network models. X-ray computed microtomography (1-4) can provide good quality volume images of the pore space. Unfortunately, this technique is not suited for routine application. Most importantly, its resolution is not sufficient to image the sub-micron size pores that are abundant in chalk. In

the absence of experimental 3D volume data, 3D stochastic reconstruction from limited statistical information obtainable from 2D microscopic images is a viable alternative. For the case of chalk, whose microstructure is too complex to reproduce by explicit modeling of the grain depositional and diagenetic processes (5), stochastic reconstruction is also the only alternative.

The conditioning and truncation of Gaussian random fields (GRF) is a widely used stochastic reconstruction technique (e.g., 6-12). The approach is mathematically elegant and computationally efficient, but unfortunately limited to imposing the void fraction (porosity) and pore-pore autocorrelation function of the reference (real) medium as the only reconstruction constraints. Much greater flexibility is offered by the simulated annealing (SA) method (13-16). Using this method, Yeong and Torquato (13) imposed the pore-phase two-point correlation and lineal path functions as constraints in the reconstruction of a Fontainebleau sandstone sample. Manwart *et al.* (14) reconstructed Berea and Fontainebleau sandstone samples from information on the pore-phase two-point correlation function, pore-phase lineal path function, and pore size distribution function. Liang *et al.* (15) imposed the "neighborhood rank" distribution together with two-point correlation function. In a recent study using the SA technique, Talukdar *et al.* (16) showed that the solid phase chord distribution function contains additional information that is critical for the reconstruction of the morphology of *particulate* media exhibiting short-range order. They confirmed this finding by successfully reconstructing the microstructure of a pack of irregular silica particles. Despite its flexibility to include an arbitrary number of reconstruction constraints, the SA method is limited by slow convergence. This makes the reconstruction of large samples (256^3 or more voxels) impractical on single-processor computers.

With the exception of a recent study by Bekri *et al.* (11), stochastic reconstruction and network modeling techniques have not been previously used in the study of chalk reservoirs. While Bekri *et al.* have demonstrated the feasibility of this approach for predicting the petrophysical properties of chalk samples, it is important to consider whether or not further refinement is possible, given recent advances in pore space characterization techniques and software (Liang *et al.*, 17). This task is undertaken in this study.

In this paper, we study stochastic replicas of the microstructure of a chalk sample generated by the GRF and SA techniques from porosity and autocorrelation function information. The paper is organized as follows. In Section 2 we briefly review the definitions of statistical functions used to describe the morphology of a microstructure and describe the algorithms used to reconstruct it from limited morphological information. In Section 3 we briefly describe the laboratory measurements conducted to determine petrophysical properties and obtain morphological parameters required as input to the reconstruction algorithms. In Section 4 we describe the reconstruction results confirming that the GRF reconstruction can be used as input to the SA method in order to refine the reconstruction and accelerate its convergence. In Section 5 we briefly describe the methods used to calculate various petrophysical properties of the chalk sample (permeability, formation factor, mercury-air capillary pressure and resistivity index vs. saturation relationships). In Section 6 we compare model predictions to experimental results. We summarize in Section 7 with concluding remarks on the significance of our findings.

2. Stochastic reconstruction from limited morphological information

2.1. Morphological descriptors of the porous microstructure

The structure of a porous material is completely defined in terms of the binary phase function $Z(\vec{r})$, which takes the value of unity if a point \vec{r} in space belongs to the void phase and the value of zero otherwise. For a statistically homogeneous medium, the void fraction (porosity),

\mathbf{f} , and the autocorrelation function of the void phase, $R_z(\bar{u})$, are formally defined as the first two statistical moments of the function $Z(\bar{r})$,

$$\mathbf{f} = \langle Z(\bar{r}) \rangle, \quad [1]$$

$$R_z(\bar{u}) = \frac{\langle [Z(\bar{r}) - \mathbf{f}] \cdot [Z(\bar{r} + \bar{u}) - \mathbf{f}] \rangle}{\mathbf{f} - \mathbf{f}^2}, \quad [2]$$

where angular brackets denote statistical averages and \bar{u} is a lag vector. For an isotropic porous medium, \mathbf{f} is a constant and $R_z(\bar{u})$ is only a function of the modulus of the lag vector, *i.e.*, $R_z(\bar{u}) = R_z(u)$. The function $R_z(u)$ may be determined from cross-sectional images of the pore space or from small-angle scattering experiments. Its slope at the origin is related to the specific surface area (the interfacial area per unit volume) s , which for digitized media is given by (13):

$$s = -6(\mathbf{f} - \mathbf{f}^2) \left. \frac{dR_z}{du} \right|_{u=0}. \quad [3]$$

Another important morphological descriptor is the correlation length \bar{I} , which is defined as the integral of the autocorrelation function,

$$\bar{I} = \int_0^{\infty} R_z(u) du. \quad [4]$$

2.2. Reconstruction of porous media by the Gaussian Random Field method

Detailed descriptions of the GRF technique may be found elsewhere (e.g., 6-8). Briefly, the method utilizes as input the target porosity \mathbf{f} and the void phase autocorrelation function $R_z(\bar{u})$, calculated from binary 2D images of the real chalk sample (cf. Eqs. [1]-[2]). The latter function is computed along the two orthogonal directions only. The basic idea behind the GRF method is to generate values of the phase function $Z(\bar{r})$ on a cubic grid of fixed size (e.g., 256^3 voxels) in a manner that satisfies the target porosity and autocorrelation function. The reconstruction starts from a realization of a continuous 3D uncorrelated Gaussian field. This uncorrelated field is subsequently passed through a linear filter that introduces spatial correlation. The linear filter is constructed from the target porosity and autocorrelation function so that the requisite binary field $Z(\bar{r})$ is obtained by a final thresholding operation.

2.3. Reconstruction of porous media by the Simulated Annealing method

The stochastic reconstruction of porous media by simulated annealing has been advanced by Yeong and Torquato (13). The main idea behind this simple but powerful technique is to gradually transform an unstructured ("high-energy") configuration of solid and void pixels into a "minimum-energy" configuration, where "energy" is measured in terms of deviations from a set of target, experimentally determined, functions conveying morphological information, *e.g.*, $R_z(u)$. This is a stochastic optimization problem with an objective function generally defined in terms of n reference functions as:

$$E = \sum_n \sum_{u=0}^{u_n^{\max}} [f_n(u) - \tilde{f}_n(u)]^2, \quad [4]$$

where, f_n and \tilde{f}_n are the simulated and reference functions, respectively. For the purposes of this work, the reference functions imposed are the pore-pore autocorrelation functions along the three orthogonal directions, $R_{z_x}(u)$, $R_{z_y}(u)$ and $R_{z_z}(u)$. Each reference function \tilde{f}_n is matched to a maximum lag u_n^{max} .

The simulation begins by randomly designating fractions f and $(1-f)$ of void and solid phase pixels, respectively, on a grid of size N^3 . At each iteration step k , a void and a solid pixel are chosen at random and their phase function values are interchanged. This interchange slightly modifies the functions f_n and therefore changes the energy of the system while preserving the porosity. A pixel interchange is accepted with a probability p_a given by the Metropolis rule (18),

$$p_a^{(k)} = \begin{cases} 1 & \text{if } DE^{(k)} \leq 0 \\ e^{-DE^{(k)}/T^{(k)}} & \text{if } DE^{(k)} > 0 \end{cases}, \quad [5]$$

where $DE^{(k)} = E^{(k+1)} - E^{(k)}$ and $T^{(k)}$ is a control parameter representing the "temperature" of the system (13). The starting value and the rate of reduction of T are governed by an *annealing schedule*. This schedule should be such that a global optimum is achieved as quickly as possible. In practice, T is reduced by a factor I after a predefined number of interchanges, referred to as a *Markov chain*. If rapid convergence is expected, a dynamic schedule, which takes into account the rapid fluctuations in the evolving energy in updating the system temperature T should be preferred over a static one where T decreases monotonically. Otherwise, there is a real possibility that the system will be trapped at a local energy minimum, unless T is decreased very slowly. The following formula for updating T was adopted in this work (19):

$$I = \text{Max} \left[I_{min}, \text{Min} \left(I_{max}, \frac{E_{min}}{E} \right) \right], \quad [6]$$

where I_{min} and I_{max} are the minimum and maximum allowable reduction factors, respectively, and are specified by the user. In this approach, for each *Markov chain*, the lowest and average energy values reached, E_{min} and \bar{E} , are used to compute the reduction factor I . The system temperature is then updated as,

$$T = T_o e^{(1-I)(m+1)}, \quad [7]$$

where, T_o is the starting temperature and m is the number of Markov chains after a total of k interchanges. This approach permits estimation of the starting temperature from the initial behavior of the energy function. Accordingly, the mean change in the energy function for k_o initial iterations is first evaluated:

$$\overline{DE} = \frac{1}{k_o} \sum_{k=1}^{k_o} DE^{(k)}. \quad [8]$$

The starting temperature T_o is then estimated from the following expression for a given initial acceptance probability p_a^o ,

$$p_a^o = e^{-\overline{DE}/T_o}. \quad [9]$$

All results obtained in this work were obtained with $k_o = 100$, $p_a^o = 0.5$ and $m = 11500$. It should be kept in mind that the choice of these parameters is highly system-specific (19).

2.4. Hybrid GRF/SA reconstruction

The simulated annealing algorithm is very slow because of the large number of unsuccessful voxel interchanges, especially at low temperatures. For comparison, a GRF reconstruction of size 256^3 takes only a little more than an hour on a lightly loaded IBM RS6000 UNIX workstation, whereas a SA reconstruction of this size takes several days. From the point of view of obtaining a realistic replica of a microstructure, the SA method is, however, preferred because it can accommodate additional reconstruction constraints. It is therefore worth exploring the potential time saving that may arise from initiating the SA reconstruction with a GRF-generated instead of a random configuration.

3. Laboratory measurements

3.1. Target image and morphological parameters

The GRF and SA methods were used to reconstruct a high porosity, low permeability North Sea chalk sample. The reference (target) porosity and autocorrelation function were obtained from a single backscatter SEM image of size 512×512 pixels, acquired at $1500\times$ magnification and providing a pixel resolution of $0.136 \times 0.136 \mu\text{m}^2$. The image was captured from a thin section of approximate size $10 \times 10 \times 1 \text{ mm}^3$ that was cut off from a cleaned and dried core sample and then impregnated with epoxy under vacuum. A binary image was obtained by setting all pixels above a threshold value to zero (Fig. 1a). The porosity of the binary image was 0.309. The target autocorrelation function was calculated from the two-point correlation function $S_2(u)$ from the equation:

$$R_z(u) = \frac{S_2(u) - f^2}{(f - f^2)}. \quad [10]$$

This function was calculated along the two orthogonal directions. The x- and y-direction autocorrelation functions are shown in Fig. 1(b) together with the average. The average autocorrelation function for this sample corresponds well with those reported by Bekri *et al.* (11) for similar North Sea chalk samples.

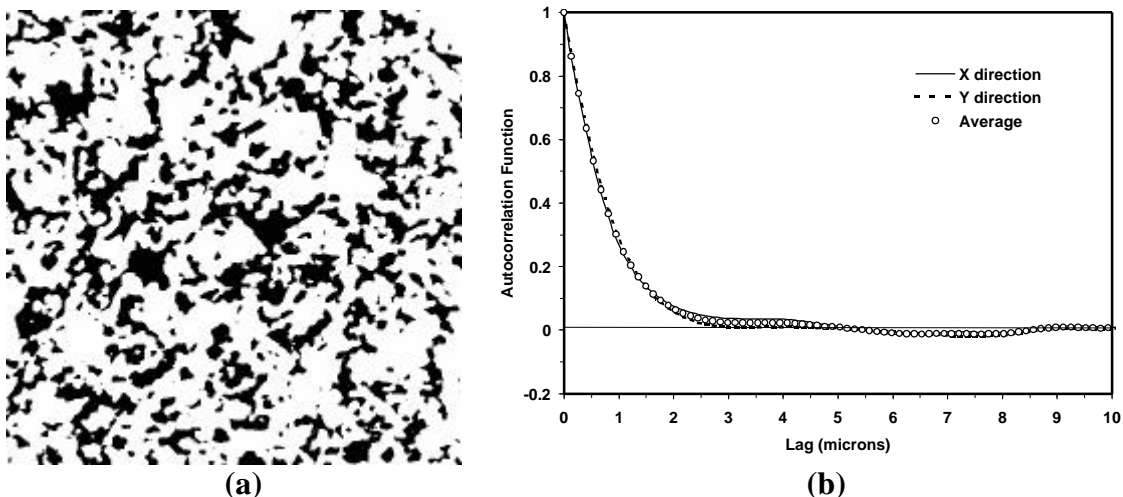


Fig. 1—(a) Back-scatter SEM image of a North Sea chalk sample. Image size is 512×512 pixels ($70 \times 70 \mu\text{m}^2$). The image is thresholded segmenting pore (black) and solid (white). Image porosity is 0.309. (b) Autocorrelation function of the image.

The correlation length was calculated using Eq. [4] and found equal to 6.68 pixels or 0.91 μm , a value close to those reported by Bekri *et al.* (11). The specific surface area of the sample calculated from the binary image using Eq. [3] is 1.3 μm^{-1} . This value differs significantly from the value obtained by mercury intrusion porosimetry (MIP), which is 4.75 μm^{-1} . This discrepancy is expected, considering the limited resolution (0.136 $\mu\text{m}/\text{pixel}$) of the image data. The magnitude of specific surface area is dependent on the size of the "probe" used to measure it. Since MIP detects pore volume invaded at capillary pressures corresponding to equivalent cylindrical pore radii smaller than 0.136 μm , it is expected that MIP will yield a higher specific surface area.

3.2. Petrophysical properties

Porosity, absolute permeability and capillary pressure were measured in the laboratory using standard laboratory equipment. The porosity of the chalk sample was measured on standard size dry core using a helium porosimeter and found equal to 0.3, in good agreement with the image data. A constant head permeameter with a Hassler cell was used to measure the permeability to air and brine. The absolute air and brine permeabilities were 1.35 mD and 0.64 mD, respectively. The brine permeability was measured using formation brine saturated with calcite to avoid dissolution of chalk in the brine and is believed that deposition of calcite on pore walls may have contributed to the lower permeability to brine.

The oil (decane)-water (formation brine) capillary pressure was measured in a centrifuge (Beckman Model LH-M Ultracentrifuge). The drainage capillary pressure curve is shown in Fig. 2. The residual water saturation is shown to be about 0.3 at $P_c \approx 5$ bar, the maximum capillary pressure reached in the centrifuge without core damage. This value is considerably higher than 0.1, the value typical attributed to the "irreducible" water saturation of North Sea chalk. Mercury porosimetry measurements were conducted using a Carlo Erba Porosimeter 2000. Before the measurement, the chalk sample was dried for about one day at 60°C. It was then evacuated to a pressure below 10^{-4} mm Hg until a constant weight at room temperature was observed. The mercury-air capillary pressure was calculated from intrusion mercury volume versus pressure data and is included in Fig. 2. The two curves cannot be brought into coincidence by scaling with the ratio of the product $s \cos \theta$ of the two fluid pairs. This indicates significant differences in fluid distribution at the pore scale for the same value of wetting fluid saturation.

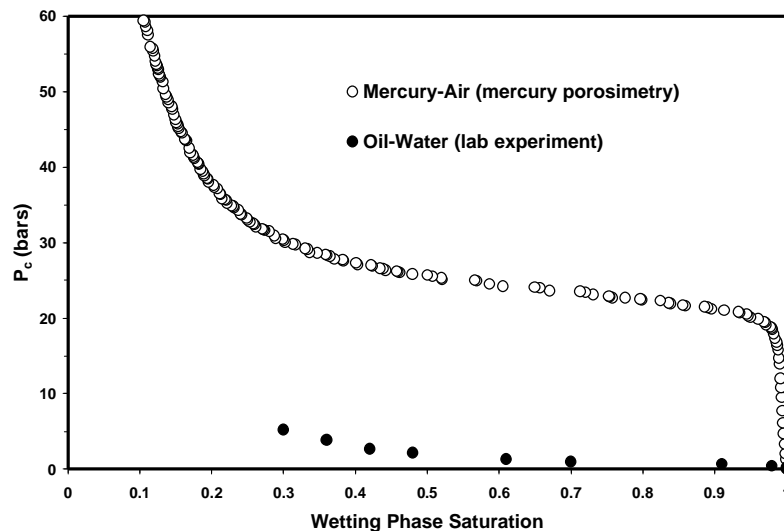


Fig. 2—Oil-water and mercury-air capillary pressures of the target chalk sample obtained from centrifuge and mercury porosimetry measurements respectively.

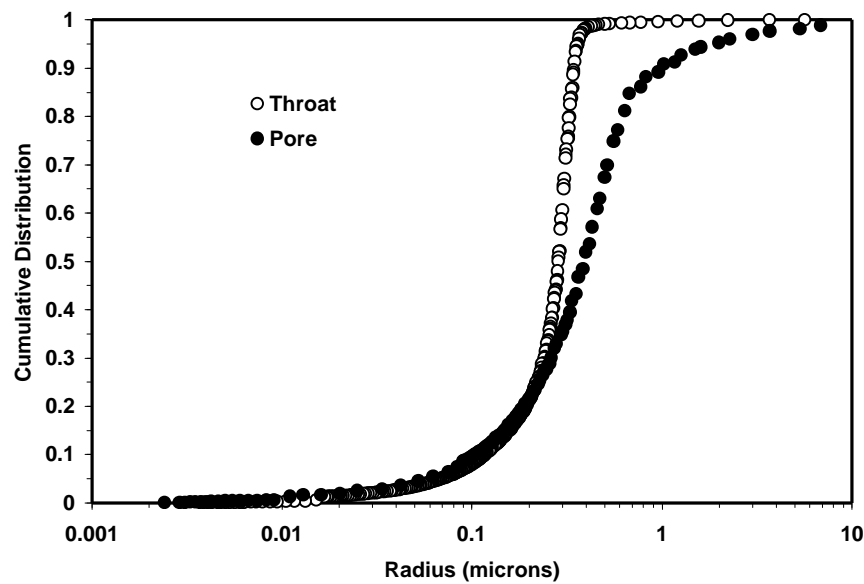


Fig. 3—Pore and throat size distributions of the target chalk sample obtained from mercury porosimetry measurement assuming pores and throats have cylindrical shape. Mean throat and pore radii are 0.27 and 0.73 μm respectively.

Mercury intrusion and extrusion data provide information about the sizes of throats and pores in the chalk sample. The cumulative distribution of pore volume by pore throat size is obtained from the intrusion data. Similarly, the retraction data provide an estimate of the cumulative distribution of pore volume by pore size. It is understood that these estimates are compromised by pore space accessibility limitations and, for the case of retraction data, permanent trapping of mercury (20). An equivalent cylindrical capillary radius is obtained from capillary pressure. The relationship of radius of pore or throat with capillary pressure is expressed by the well-known Young-Laplace equation of capillarity,

$$P_c = \frac{2 \sigma \cos \theta}{r}, \quad [11]$$

where, r is the pore or throat radius, σ is the mercury surface tension, θ is the contact angle and P_c is the retraction or intrusion capillary pressure. The pore and throat radius distributions are calculated considering a surface tension of 480 dyne/cm and a contact angle of 140° for intrusion and 120° for extrusion. The resulting distributions are shown in Fig. 3. As can be observed, there is considerable overlap between the pore and throat sizes. The mean radius of the throat size distribution is 0.27 μm and that for pore size distribution is 0.73 μm .

4. Reconstruction results

4.1. GRF and SA reconstructions of a 100^3 sample

The potential of hybrid GRF/SA reconstruction was tested on a sample containing 100^3 voxels. Three cases were considered. In Case 1, the SA method is used with an initial configuration that corresponds to a cube of size 100^3 voxels extracted from a GRF-generated realization of size 256^3 voxels. In this case annealing was started at high initial temperature allowing the system to "melt". Case 2 differs from Case 1 in that annealing was started at low initial temperature preventing "melting" of the system. The initial energy for Cases 1 and 2 was 0.322 and the reconstruction was completed as soon as the energy fell below 10^{-5} (see Table 1). In Case 3, the conventional SA method was applied, with the annealing process starting at high initial temperature from a random, uncorrelated configuration.

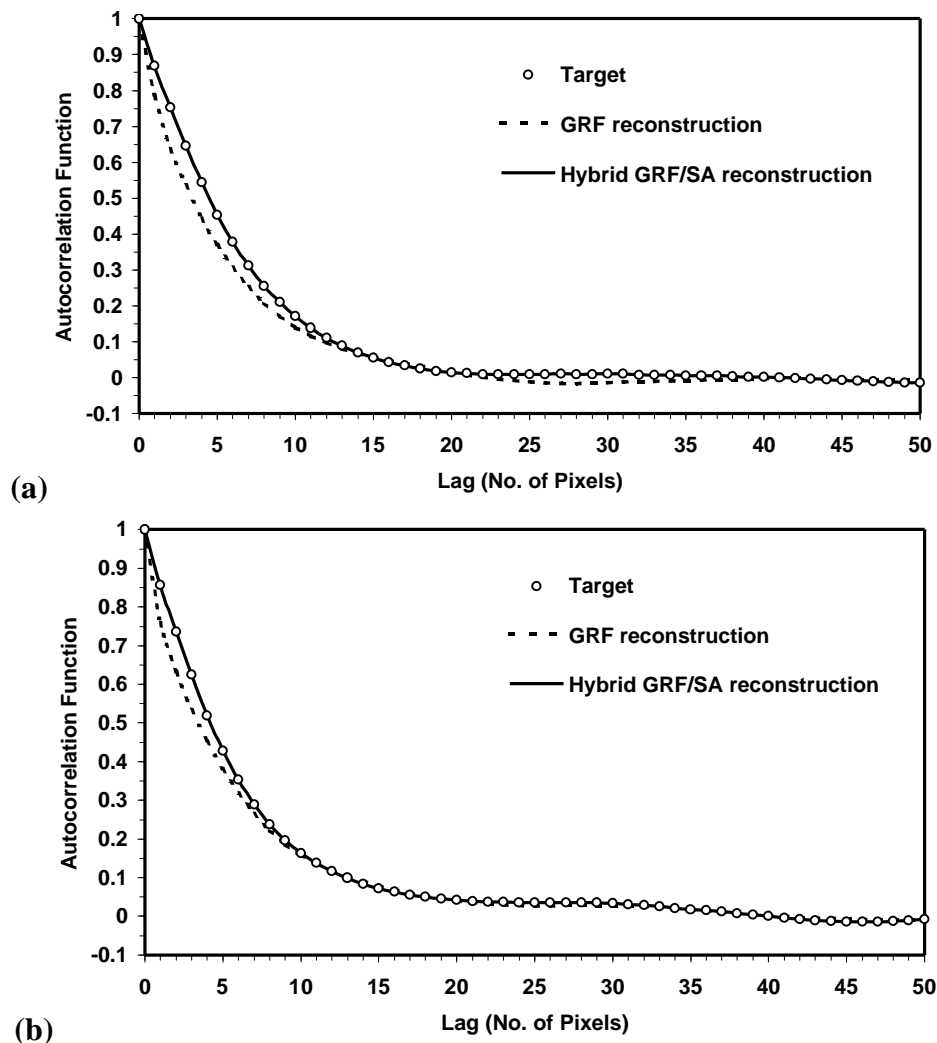


Fig. 4—Target and reconstructed (100^3 sample) autocorrelation functions; (a) x-direction; (b) y-direction. Empty circles represent target autocorrelation function, broken and solid lines represent autocorrelation functions of the GRF-generated and hybrid GRF/SA-generated (Case 2) media respectively.

As a result of further reduction of energy in the system by SA method, improved match of the autocorrelation functions in all directions is observed for Cases 1 and 2 by comparison to the initial, GRF-generated configuration (see Fig. 4). Note that the initial configuration (a sub-volume from a GRF-generated realization of size 256^3 voxels) does not match the target functions, whereas the complete (256^3 voxels) GRF realization does (see below).

The reduction of energy in the system by SA yields better reconstruction. Fig. 5 presents sections through the reconstructed microstructures for the three cases. A section of the target image (taken from Fig. 1(a)) is shown for comparison in Fig. 5(a). Visually, the images look alike, but a closer inspection reveals subtle differences in the shape of the rock-pore interface and the number of small void and solid features.

The evolution of energy and temperature for the three cases is presented in Fig. 6. For Case 2 and Case 3, a nearly exponential decrease in energy and temperature is observed. For Case 1, however, the energy initially builds up in the system as the system "melts" during cooling. Notice how temperature fluctuates during the energy build up. This is due to the dynamic nature of the annealing schedule, which takes into account the abrupt changes in the evolving energy function.

From the point of view of computational efficiency, initialization of SA with a GRF-generated, instead of an uncorrelated random configuration, seems promising. Table 1 shows some of the important simulated annealing parameters. The simulations were performed on an IBM RS6000 SP Model 9076-260 computer. The conventional SA reconstruction required 5.89 CPU hours (22.7 million iterations) to reconstruct a 100^3 sample, but only 3.88 hours (15.7 million iterations) when the annealing process was started from GRF reconstruction at low initial temperature. For a larger model (e.g., 256^3 voxels), the savings in CPU time would be considerably more significant. It should be noted here that there is no gain if the annealing process is started at high initial temperature.

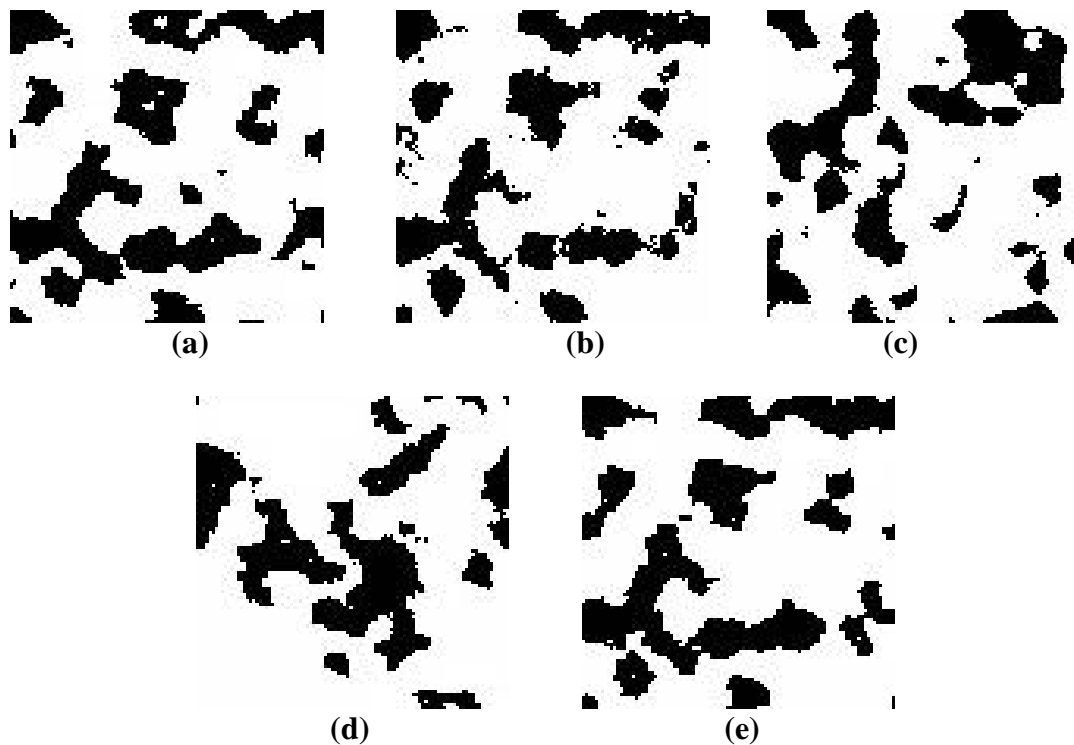


Fig. 5—Reconstruction of 100^3 sample; (a) target image (100x100 pixels taken from Fig. 1(a)). Typical sections through reconstructed media; (b) GRF-generated; (c) hybrid GRF/SA (Case 1); (d) hybrid GRF/SA (Case 2); (e) Conventional SA (Case 3). Pores are in black.

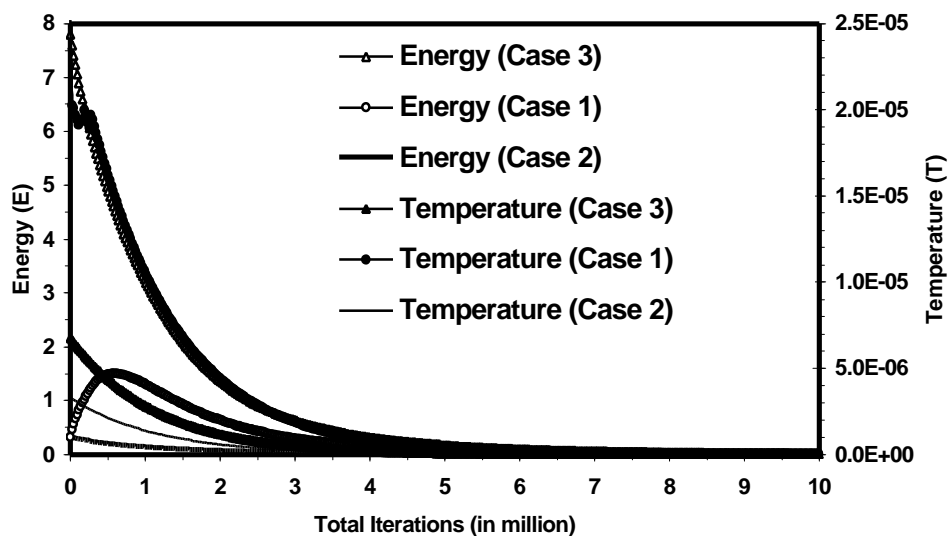
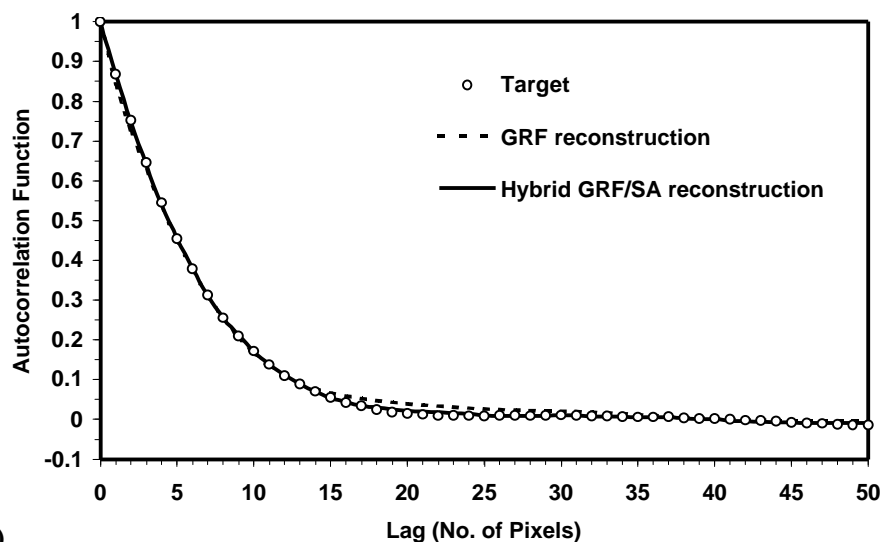


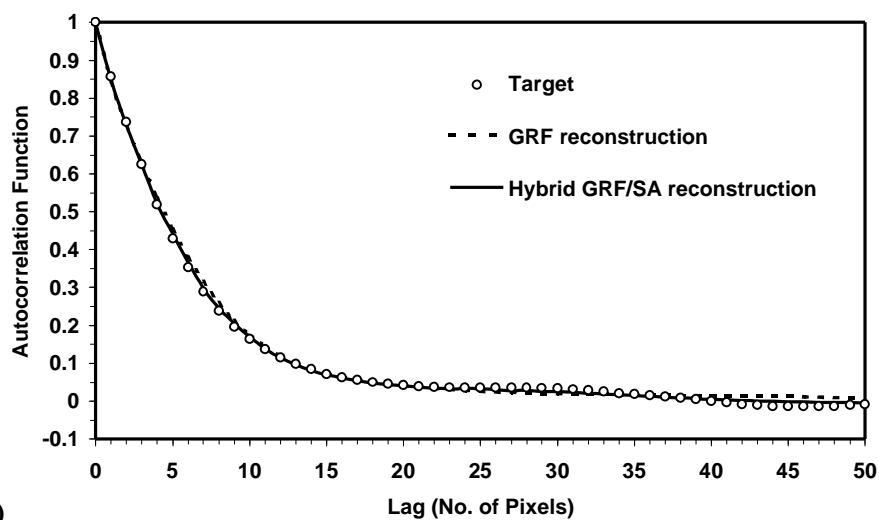
Fig. 6—Evolution of energy and temperature for the three simulated annealing reconstruction cases (Case 1, 2 and 3). For clarity, volume of data has been reduced.

Table 1—Comparison of the SA parameters for construction of a 100^3 sample

	Simulated annealing reconstruction cases (target energy 10^{-5})		
	Case 1	Case 2	Case 3
Energy at start	0.322	0.322	7.80
Temperature at start	2.52E-05	3.30E-06	6.76E-06
CPU time (hours)	5.68	3.88	5.89
Total iterations (millions)	22.37	15.70	22.70
Convergence temperature	7.27E-17	1.29E-14	3.64E-17



(a)



(b)

Fig. 7—Target and reconstructed (256^3 sample) autocorrelation functions; (a) x-direction; (b) y-direction. Empty circles represent target autocorrelation function, broken and solid lines represent autocorrelation functions of the GRF-generated (Case 4) and hybrid GRF/SA-generated (Case 5) media respectively.

4.2. GRF and SA reconstructions of a 256^3 sample

A reconstructed porous medium of size 100^3 voxels is not sufficiently large for obtaining reliable estimates of macroscopic properties, such as, permeability, resistivity index etc. For this reason, two realizations of size 256^3 voxels were generated. The first one (Case 4) was reconstructed using the GRF method. Reconstruction of this size by SA method even using only autocorrelation function seems impractical at the present time due to limitations in computer speed. We therefore adopted the new hybrid technique described in Section 2.4 and

exemplified in Section 4.1 (Case 2). We refer to this realization as Case 5. The starting energy (after GRF reconstruction) calculated from Eq. 4 was 0.0283. We reduced this energy by an order of magnitude (0.0026) in about 9 hours on an IBM RS6000 SP Model 9076-260 computer. Since the annealing was started at low initial temperature, the energy decreased gradually and no "melting" took place. For this modest reduction in energy, we observed an improved match of the autocorrelation function (see Fig. 7) and a "smoother" image (see Fig. 8). A 3D representation of the reconstructed chalk (Case 5) is shown in Fig. 9.

It is interesting to note how other measures of the morphology of the chalk microstructure, not imposed as constraints on the reconstruction process, are reproduced in the models. Application of the SA method provided a better match between the chord distribution functions of the target image and the reconstructed sample. Fig. 10 shows solid- and pore-phase chord distribution functions along the x-direction for the target image and the two reconstructed samples (Cases 4 and 5). Similar results were obtained in other directions and hence not shown.

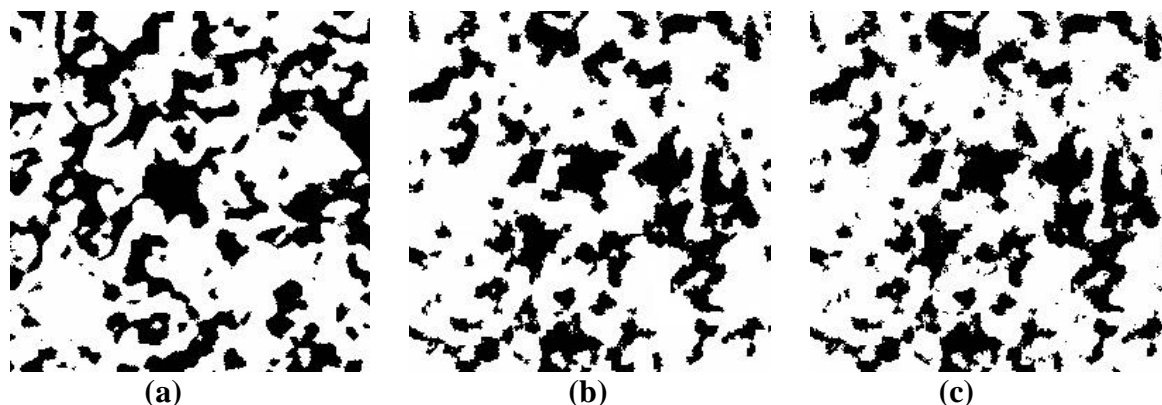


Fig. 8—Reconstruction of 256^3 sample; (a) target image (256x256 pixels taken from Fig. 1(a)). Typical sections through reconstructed media; (b) GRF-generated (Case 4); (c) hybrid GRF/SA-generated (Case 5). Pores are in black.

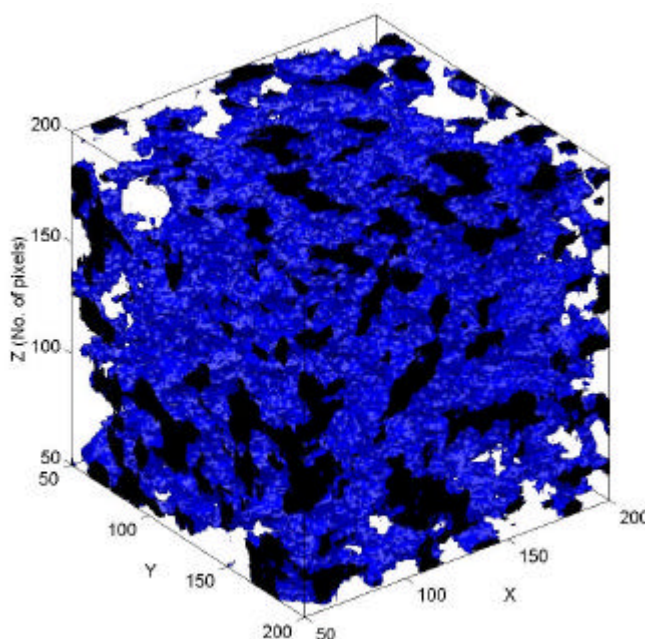


Fig. 9—Pore spaces (blue) of the reconstructed chalk sample (Case 5). A subvolume of 150^3 pixels has been shown. The end caps of the pore spaces are shown in black.

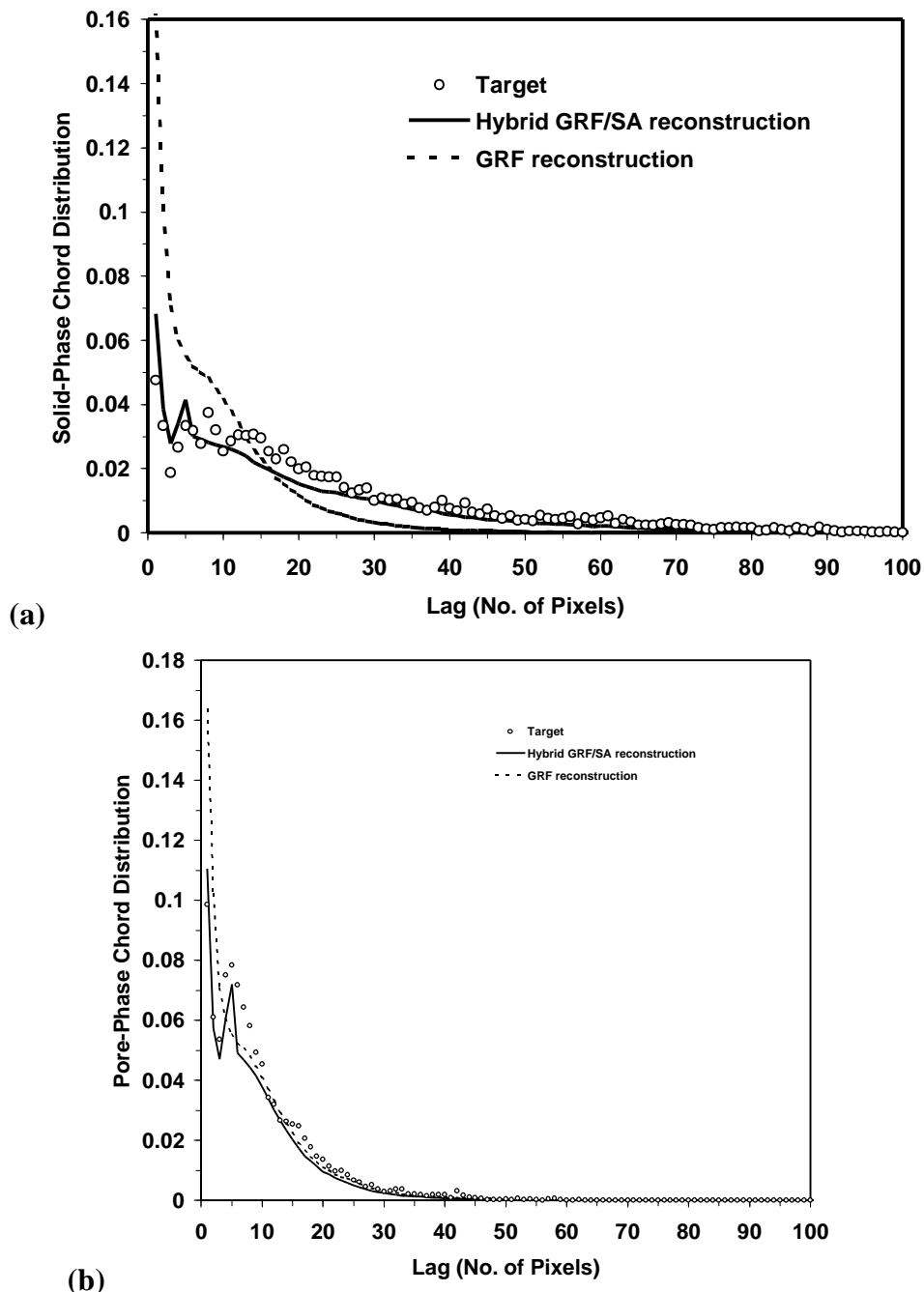


Fig. 10—Chord distribution functions of the reconstructed sample (256^3) in x-direction; (a) solid phase; (b) pore phase. Empty circles represent target chord distribution, broken and solid lines represent chord distributions of the GRF-generated (Case 4) and hybrid GRF/SA-generated (Case 5) media respectively.

5. Network modeling for petrophysical property estimation

5.1. Characterization of the reconstructed media

The stochastic reconstruction techniques applied in this study do not impose any connectivity constraints. Therefore, the reconstructed media may contain clusters of isolated pore and solid pixels. These isolated clusters contribute to the correlation functions and their removal by filtering results in deviations from the target functions. This afflicts reconstructed media for which $f < 0.2$ (8) and is not a matter of concern in the reconstruction of chalk. Nonetheless, the cluster reconnection algorithm of Liang *et al.* (15) was implemented to establish the connectivity of the void phase. The algorithm conserves porosity and causes negligible

changes to the morphology of the solid-void interface and autocorrelation function. We found 0.3% isolated pore pixels in the medium reconstructed by the GRF technique (Case 4) and 0.1% in the medium reconstructed medium by the hybrid GRF/SA technique (Case 5).

The fully connected media were characterized using the pore space partitioning algorithms developed by Liang *et al.* (17). The method is based on partitioning of pore space into nodal pores by identifying local minima in the cross-sectional area of the pore space channels using a skeleton link scanning procedure. The methodology takes advantage of a 3D, connectivity preserving, fully parallel thinning algorithm developed by Ma and Sonka (21). The thinning algorithm is used to extract the skeleton (medial axis) of the pore space. The skeleton serves as the basis for characterization of the reconstructed media. The characterization provides the distributions of pore volume V_p , throat area A_t , throat hydraulic radius R_H and coordination number, as well as the distributions of hydraulic and electrical conductance of distinct pore space channels.

Assuming that the pores are cubic and that the throats have a square cross-section, the pore volume and throat area distributions were converted to equivalent pore and throat sizes using the following relationships,

$$R_p = \left(\frac{V_p}{8} \right)^{1/3} \quad [11]$$

$$R_t = \left(\frac{A_t}{4} \right)^{1/2} \quad [12]$$

The pore-size, throat-size and coordination number distributions obtained from 3D characterization of the reconstructed 256^3 sample (Case 4) are shown in Figs. 11, 12 and 13 respectively. The pore and throat radii were calculated using Eq. 11 and 12 respectively. The throat-size and coordination number distributions obtained from 3D characterization of sample reconstructed in Case 5 are included in Figs. 12 and 13 respectively. The pore- and throat-size distributions calculated from mercury intrusion and extrusion data are also included in Figs. 11 and 12 respectively. As expected, the throat-size and coordination number distribution of the reconstructed sample in Case 4 differs only slightly from those of the reconstructed sample in Case 5.

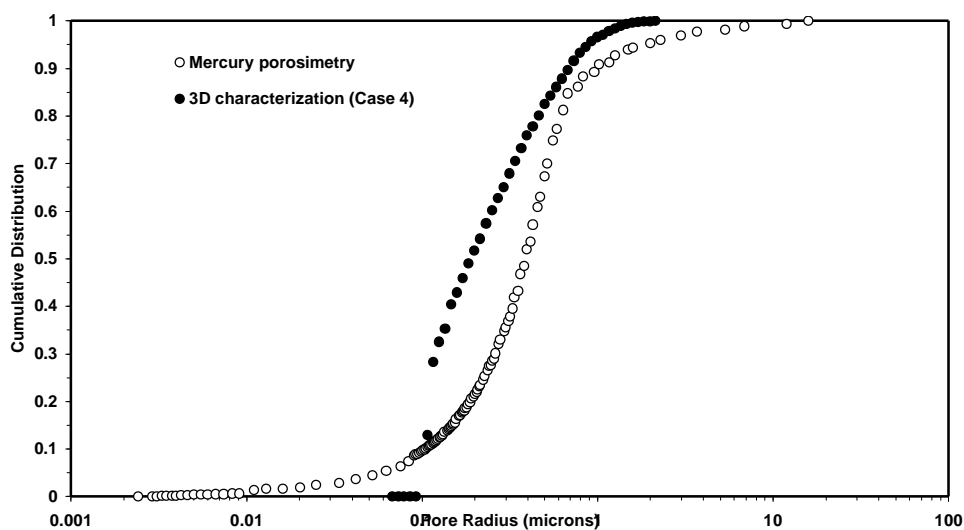


Fig. 11—Pore size distributions from mercury porosimetry and from 3D characterization of the reconstructed medium (Case 4).

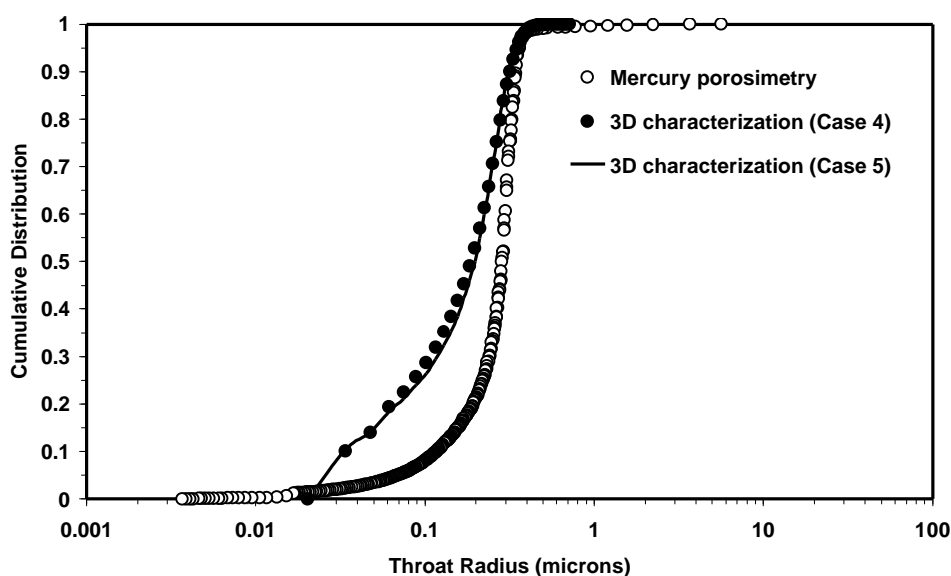


Fig. 12—Throat size distributions from mercury porosimetry and from 3D characterization of the reconstructed media (Case 4 and 5).

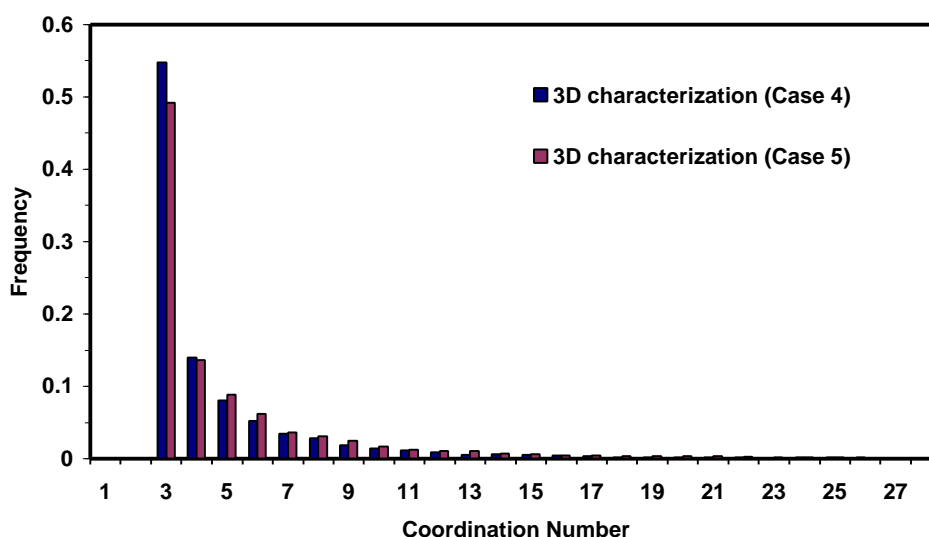


Fig. 13—Coordination number distributions of the reconstructed media (Case 4 and 5) obtained from 3D characterization.

The range of pore and throat sizes found in the reconstructed chalk sample agrees very well with the range of pore and throat sizes estimated from mercury porosimetry. This finding further supports the conclusion that stochastic reconstruction has provided a faithful replica of the chalk microstructure. As stated previously, there is no expectation that the distributions shown in Fig. 11 and Fig. 12 should overlap in anything but the range of pore and throat sizes.

The mean throat and pore radii of the reconstructed medium (Case 4) obtained from 3D characterization are 0.182 and 0.31 μm respectively. These values are somewhat lower than those obtained from mercury porosimetry data (0.27 and 0.73 μm , respectively). The mean throat radius of the reconstructed medium (Case 5) is 0.184. Samples reconstructed in Case 4 and 5 have slightly different coordination number distributions (see Fig. 13) and average values of the distributions (4.8 for Case 4 while 5.1 for Case 5). The average coordination numbers are much higher than that obtained by Bekri *et al.* (11) for similar chalk (approximately 3.2). We believe that this discrepancy is due to limitations of the

characterization methodology employed in the previous study. There are few pores having coordination number as high as 28. The 3D characterization of the reconstructed chalk (Case 4) estimated 2264 pores and 7916 necks in a sample of $35 \times 35 \times 35 \mu\text{m}^3$.

5.2. Network model

In order to estimate petrophysical properties, an equivalent network model of chalk pore structure was constructed based on bond-correlated site percolation concept detailed by Ioannidis and Chatzis (20, 22). The network model is constructed from input on porosity, average coordination number, pore- and throat-size distributions, specific surface area and shape of pores and throats. Its distinguishing features are explained below.

The network model is an approximation of the irregular 3D microstructure shown in Fig. 9. An irregular porous medium (see Fig. 14(a)) is represented by a network of cubes (pores) occupying the sites of a regular cubic lattice. The cubic pores are interconnected through volumeless throats of rectangular cross-section (see Fig. 14(b)). Prior to assignment of sizes to the sites and bonds of the lattice, site percolation is used to remove sites and associated bonds until the desired average coordination number is achieved. Next, pore sizes are randomly assigned to the lattice size from the known pore volume distribution. In agreement with detailed studies of the geometry of stochastically reconstructed porous media (23), a bias is introduced on the assignment of pore sizes so that larger pores preferentially occupy sites of greater coordination number. Assignment of throat sizes follows the bond-correlated site percolation scheme, whereby larger throats are assigned to bonds connecting larger pores. This introduces short-range spatial correlation of pore throat sizes and is also in agreement with detailed studies of the geometry of stochastically reconstructed porous media (10). The node-to-node distance, or lattice constant (l_c), is adjusted to obtain the required porosity. Note that the network model matches the average coordination number accurately, but not the coordination number distribution.

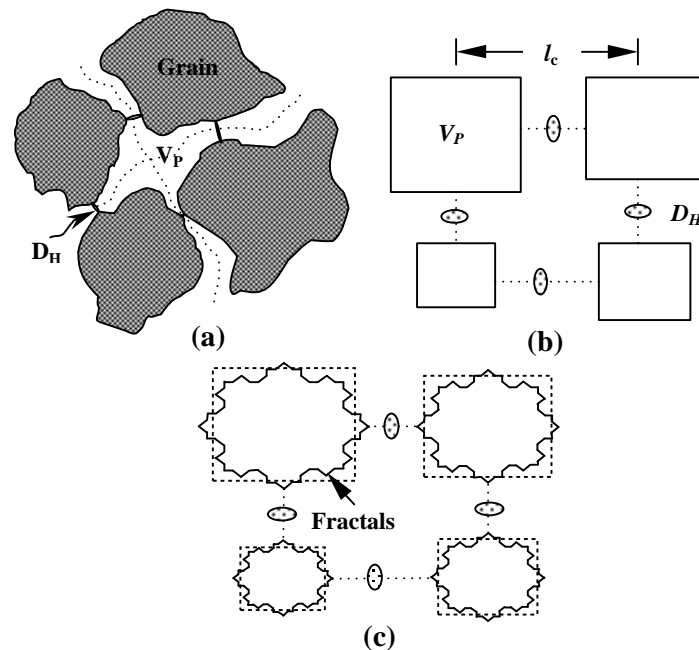


Fig. 14—Construction of a network model; (a) real porous medium; (b) equivalent network model; (c) fractal decoration in order to match specific surface area.

In the construction of the network model, it is realized that the shape of actual pores is in fact irregular (see 23). Thus, although the measured pore volume distribution is precisely matched in the network model, the model is actually smoother than the medium it is taken to represent (i.e., the specific surface area of the network model is smaller). For the sample under study the specific surface area of the equivalent network is $0.9 \mu\text{m}^{-1}$, by comparison to $1.3 \mu\text{m}^{-1}$ for the reconstructed medium and $4.75 \mu\text{m}^{-1}$ for the real sample (MIP result). Realistic simulation of immiscible displacement using the network model requires at least an approximate account of late pore filling. Several possibilities exist and the one considered here is based on a fractal "decoration" of the pores. A fractal decoration (see Fig. 14(c)) is assigned to the pore cross-section in order to match the model specific surface area (S_m) with the one measured by mercury porosimetry (S_f). It is shown (24) that the number of levels of fractal decoration (n_f) required to match this specific surface area can be expressed by,

$$n_f = \frac{\log\left(\frac{S_f}{S_m}\right)}{\log\left(\frac{4}{3}\right)} \quad [14]$$

Addition of fractal decoration increases the model pore volume. As a result, it is necessary to adjust the equivalent pore radii (Eq. 11). The volume adjustment necessary may be calculated using Eq. 15.

$$\frac{V_f}{V_p} = 1 + \frac{3}{5} \cos\left(\frac{p}{6}\right) \left[1 - \left(\frac{4}{9}\right)^{n_f} \right] \quad [15]$$

where V_f is the volume of each pore after n_f levels of fractal decoration.

5.3. Computation of petrophysical properties

Computation of absolute permeability and formation factor is based on an electric analogue-linear network concept detailed by Ioannidis and Chatzis (20, 22). To simulate fluid or current flow, one needs to compute the overall hydraulic or electric conductance of the network by applying the principle of mass or electric current balance at all nodes. In our network model the throats have no volume as they correspond to local minima in the hydraulic radius of distinct, irregularly shaped pore space channels. The equivalent hydraulic or electrical conductance of the each resistor in the network model is calculated from the following equations:

$$g_h = \frac{x R_t^4}{8 l_e} f(x) \quad [17]$$

$$g_e = \frac{4 x R_t^2}{l_e} \quad [18]$$

where l_e is an equivalent length estimated as

$$l_{e_{m-n}} = l_c - (R_{p_m} + R_{p_n}) \quad [19]$$

In these equations, $f(x)$ is a function of the throat aspect ratio ($x = l$ here) and R_{p_m}, R_{p_n} are the sizes of adjacent pores.

The mass (or electric current) balance requires that,

$$\sum q_{ij} = 0 \quad [21]$$

i.e., the algebraic sum of flows at all nodes in the network be zero. These equations together with appropriate initial and boundary conditions constitute a set of linear equations, which can be solved by a linear solver. We employed a preconditioned conjugate gradients method.

The pressure differential (DP) (or voltage differential, DV) across the model can be computed for a given volumetric flow rate (Q) (or electric current, I), enabling the calculation of the absolute permeability (k) and formation factor (F) of the network. Absolute permeability is calculated from familiar Darcy's equation:

$$k = \frac{\mu L Q}{A \Delta P} \quad [22]$$

where L is the network length and A is the network cross-sectional area. The formation factor is calculated in a similar manner.

To compute the resistivity index we simulate the process of drainage of the conductive wetting phase by a non-conductive non-wetting phase using an invasion percolation algorithm. Trapping of the wetting phase is not considered, for it is assumed that the wetting phase maintains its continuity through the corners of the pores and therefore can be drained to arbitrarily low levels by increasing the applied capillary pressure. At each stage of the drainage process, we first determine the fluid occupancy of pore and throats. The effective electrical conductivity of the pore network is computed by solving the equivalent resistor network equations. The conductance of throats invaded by the non-wetting phase is computed from the equation,

$$g_e = \frac{A_w}{l_e} \quad [23]$$

where A_w is the cross-sectional area of the pore throat that is occupied by the wetting phase. Details on the computation of the capillary pressure for invasion of the non-wetting phase into throats of rectangular cross-section and on the computation of A_w as a function of capillary pressure are given by Ioannidis and Chatzis (22).

It is emphasized that the network model is only an approximation of the pore space in chalk. The quality of this approximation must be judged not by comparing the predicted petrophysical properties with experimental data, but also by comparing them with predictions obtained using the reconstructed microstructure itself. For this reason, we also compute the permeability of the reconstructed chalk by solving the equivalent resistor network problem as described in Liang *et al* (10) and the formation factor by random-walk simulation (8).

6. Network modeling results

6.1. Capillary pressure

The network was constructed based on the 3D characterization data for the reconstructed chalk sample corresponding to Case 4. The mercury-air drainage capillary pressure computed using the network model is compared to the experimental one in Fig. 15. The network model predicts a breakthrough capillary pressure and radius of 24.5 bar and 0.29 μm respectively. The agreement is remarkably good considering the approximate nature of the network model and the fact that no adjustable parameters were used. The discrepancy in the range 30-100 bar is most likely due to the fact that the fraction of the volume of each pore that is contributed by fractal decoration (and therefore contributes to late filling) is small. Clearly, a more versatile model of late pore filling is needed (25).

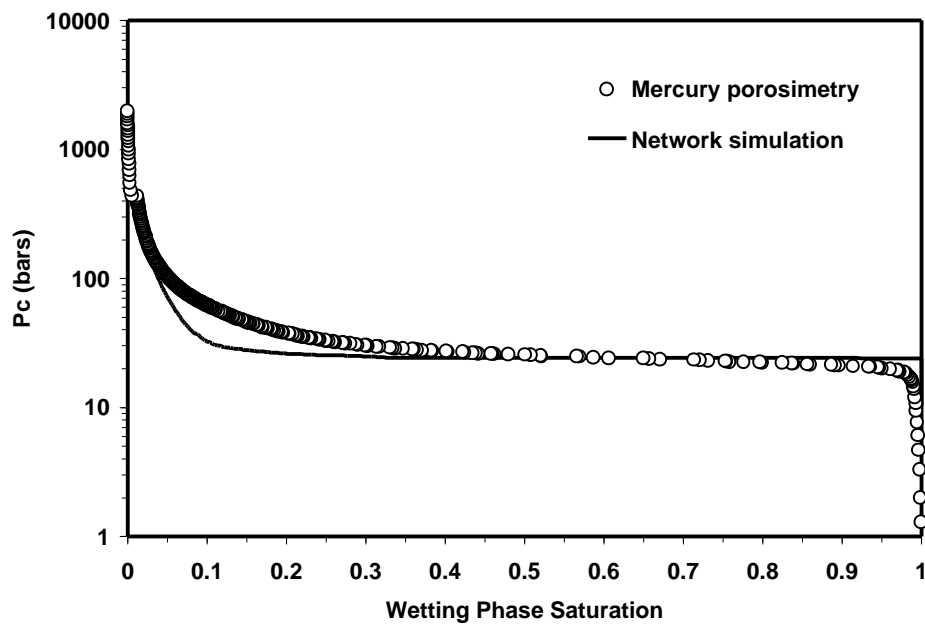


Fig. 15—Experimental and simulated mercury-air capillary pressure curves.

6.2. Absolute permeability and formation factor

Computations of absolute permeability and formation factor performed directly on the reconstructed microstructure yielded the values 1.73 mD and 12.3 respectively. The computed permeability is remarkably close to the experimental value (1.35 mD), supporting the conclusion that stochastic reconstruction has rendered the microstructure of the real sample with sufficient accuracy. The predicted formation factor is also in good agreement with experimental values for similar North Sea chalk samples reported by Bekri *et al.* (11). The predictions of permeability and formation factor from the network model are 0.643 mD and 13.5, respectively, also in good agreement. The permeability and formation factor predicted from simulation directly on the reconstructed microstructure should be considered more reliable, because the convergent-divergent geometry and exact spatial arrangement of all flow paths is taken into account. On the other hand, the network model considers flow paths as channels of uniform cross-section and slightly underestimates the hydraulic and electrical conductivity. However, the network model is computationally much more efficient and can provide estimates of petrophysical properties such as the capillary pressure and resistivity index curves, which are difficult to obtain directly from the simulated microstructure.

Finally, it is interesting to check whether the following formula, relating the values of k and F in stochastically reconstructed media to image statistical properties (f and s) (10), also holds for the reconstructed chalk:

$$k = \frac{64f^2}{226Fs^2} \quad [24]$$

Using $f = 0.309$, $s = 1.3 \mu\text{m}^{-1}$ and $F = 12.3$, we obtain $k = 1.3$ mD in excellent agreement with the measured permeability.

6.3. Resistivity index

Resistivity index is a useful quantity which, when combined with a saturation model, enables us to calculate fluid saturations in the system. Results in this study have been based on Archie's-saturation model. The basic equation relating wetting phase saturation (S_w) and resistivity index (I_r) is as follows:

$$I_r = \frac{R_t}{R_o} = S_w^{-n} \quad [25]$$

where, R_t and R_o are the resistivity indices when the system is partially and fully saturated with wetting fluid respectively, and n is the saturation exponent.

The network model described previously was used to calculate the resistivity index and saturation exponent as function of wetting phase saturation. These results are shown in Fig. 16. No experimental data are available to compare with the simulated curves.

Conclusions

The combination of Gaussian random field (GRF) and simulated annealing (SA) reconstruction techniques was studied for the first time. Hybrid GRF/SA reconstruction was shown to lead to refinement of the simulated microstructure and considerable acceleration of the convergence of the SA method. The method was used to reconstruct the microstructure of a North Sea chalk sample. Subsequent morphological, geometric and topological characterization showed that the resulting stochastic replica is a reasonably accurate model of the microstructure of the real sample. This was further confirmed by computing the permeability and formation factor of the simulated microstructure. A network model capable of incorporating the essential geometric, topological and correlational aspects of stochastically reconstructed porous media was constructed and used to estimate the petrophysical properties of North Sea chalk. The predictions of permeability, formation factor and mercury-air drainage capillary pressure curves were found to be in good agreement with experimental data. This model was further applied to the prediction of resistivity index under conditions of drainage.

Acknowledgements

Saifullah Talukdar gratefully acknowledges the financial support by Phillips Petroleum Company Norway for his Ph.D. studies. He also acknowledges the warm reception he received from the Department of Chemical Engineering (Porous Media Laboratory), University of Waterloo, Canada during his three months research stay in 2001.

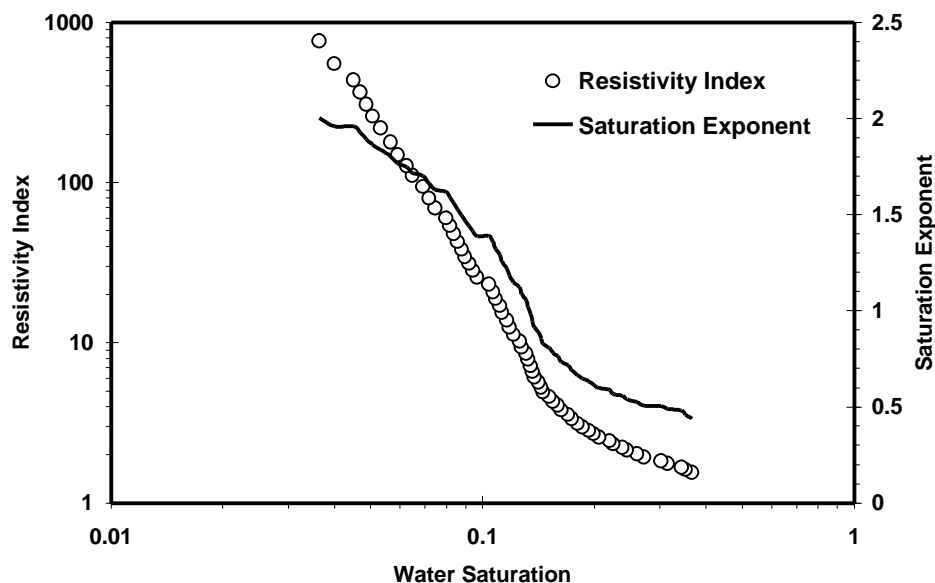


Fig. 16—Simulated resistivity index and saturation exponent (Case 4).

References

1. Spanne, P., Thovert, J., Jacquin, C., Lindquist, W., Jones, K. and Adler, P.: "Synchrotron Computed Microtomography of Porous Media: Topology and Transports," *Phys. Rev. Lett.*, **73**, 2001-2004 (1994).
2. Coles, M.E., Spanne, P., Muegge, E.L., and Jones, K.W.: "Computed Microtomography of Reservoir Core Samples," Proc. 1994 Int. Symp. of SCA, Stavanger, Norway (1994).
3. Hazlett, R.D.: "Simulation of Capillary-Dominated Displacements in Microtomographic Images of Reservoir Rocks," *Transport in Porous Media*, **20**, 21-35 (1995).
4. Coles, M.E., Hazlett, R.D., Muegge, E.L., Jones, K.W., Andrews, B., Dowd, B., Siddons, P., Peskin, A., Spanne, P. and Soll, W.E.: "Developments in Synchrotron X-Ray Microtomography with Applications to Flow in Porous Media," paper SPE 36531 presented at the 1996 Annual Technical Conference and Exhibition, Denver, Colorado, 6-9 October 1996.
5. Bakke, S. and Øren, P.E.: "3D Pore-Scale Modeling of Sandstones and Flow Simulations in the Pore Networks," *SPEJ*, **2**, 136-149 (1997).
6. Quiblier, J.A.: "A New Three-Dimensional Modeling Technique for Studying Porous Media," *J. of Colloid and Interface Science*, **98**, 84-102 (1984).
7. Adler, P.M., Jacquin, C.G. and Quiblier, J.A.: "Flow in Simulated Porous Media," *Int. J. of Multiphase Flow*, **16** (4), 691-712 (1990).
8. Ioannidis, M.A., Kwiecien, M.J., and Chatzis, I.: "Electrical Conductivity and Percolation Aspects of Statistically Homogeneous Porous Media," *Transp. Porous Media*, **29**, 61 (1997).
9. Levitz, P.: "Off-Lattice Reconstruction of Porous Media: Critical Evaluation, Geometrical Confinement and Molecular Transport," *Advances in Colloid and Interface Science*, **76/77**, 71-106 (1998).
10. Liang, Z., Ioannidis, M.A., and Chatzis, I.: "Permeability and Electrical Conductivity of Porous Media from 3D Stochastic Replicas of the Microstructure", *Chem. Eng. Sci.*, **55**, 5247 (2000).
11. Bekri, S., Xu, K., Yousefian, F., Adler, P.M., Thovert, J.-F., Muller, J., Iden, K., Psyllos, A., Stubos, A.K., and Ioannidis, M.A.: "Pore Geometry and Transport Properties in North Sea Chalk," *J. Petrol. Sci. Eng.*, **25**, 107 (2000).
12. Kainourgiakis, M.E., Kikkinides, E.S., Steriotis, Th.A., Stubos, A.K., Tzevelekos, K.P., and Kanellopoulos, N.K.: "Structural and Transport Properties of Alumina Porous Membranes from Process-Based and Statistical Reconstruction Techniques," *J. Colloid Interface Sci.*, **231**, 158 (2000).
13. Yeong, C.L.Y. and Torquato, S.: "Reconstructing Random Media. II. Three-Dimensional Media from Two-Dimensional Cuts," *Physical Review E*, **58**, 224-233 (1998).
14. Manwart, C., Torquato, S., and Hilfer, R.: "Stochastic Reconstruction of Sandstones," *Phys. Rev. E*, **62**, 893 (2000).
15. Liang, Z., Ioannidis, M.A. and Chatzis, I.: "Reconstruction of 3D Porous Media Using Simulated Annealing," Proc. of the XIII Int. Con. on Computational Methods in Water Resources, Alberta, Canada, 25-29 June 2000.
16. Talukdar, M.S., Torsaeter, O. and Ioannidis, M.A.: "Stochastic Reconstruction of Particulate Media from 2D Images," *Journal of Colloid and Interface Science*, **248**, 419-428 (2002).
17. Liang, Z., Ioannidis, M.A. and Chatzis, I.: "Geometric and Topological Analysis of Three-Dimensional Porous Media: Pore Space Partitioning Based on Morphological Skeletonization," *J. of Colloid and Interface Science*, **221**, 13-24 (2000).
18. Metropolis, N., Rosenbluth, A., Rosenbluth, M., Teller, A. and Teller, E.: "Equation of State Calculations by Fast Computing Machines," *J. Chem. Phys.*, **21**, 1087-1092 (1953).
19. Ouenes, A., Bhagavan, S., Bunge, P.H. and Travis, B.J.: "Application of Simulated Annealing and Other Global Optimization Methods to Reservoir Description: Myths and Realities," paper SPE 28415 presented at the 69th Annual Technical Conference and Exhibition, New Orleans, LA, 25-26 September 1994.
20. Ioannidis, M.A. and Chatzis, I.: "A Mixed-Percolation Model of Capillary Hysteresis and Entrapment in Mercury Porosimetry," *J. of Colloid and Interface Science*, **161**, 278 (1993).
21. Ma, C.M. and Sonka, M.: "A Fully Parallel 3D Thinning Algorithm and Its Applications," *Comput. Vision Image Understanding*, **64**, 420 (1996).
22. Ioannidis, M.A. and Chatzis, I.: "Network Modeling of Pore Structure and Transport Properties of Porous Media," *Chem. Eng. Sci.*, **48**, 951 (1993).
23. Ioannidis, M.A. and Chatzis, I.: "On the Geometry and Topology of 3D Stochastic Porous Media," *J. of Colloid and Interface Science*, **229**, 323 (2000).
24. Lowell, S. and Shields, J.E.: "Powder Surface Area and Porosity," 3rd edition, Chapman & Hall (1991).
25. Chang, D. and Ioannidis, M.A.: "Pore Network Simulation of Low-Field NMR Relaxometry Under Conditions of Drainage and Imbibition: Effects of Pore Structure and Saturation History," SCA 2001-18 presented at the 2001 International Symposium of the SCA, Edinburgh, Scotland, 17-19 September 2001.